Available online at www.sciencedirect.com
ScienceDirect
Trans. Nonferrous Met. Soc. China 35(2025) 3057−3073
Transactions of Nonferrous Metals Society of China
www.tnmsc.cn

# Rheology, curing behavior, and porosity evolution in dual curing direct ink writing of carbon/carbon composites

Xin YE[1], Qian LU[1], Lu-tong WU[1], Ming-liang XU[2], XIANG Xiong[2], Feng-ze JIANG[2]

1. College of Mechanical and Electrical Engineering, Central South University, Changsha 410083, China;
2. State Key Laboratory of Powder Metallurgy, Central South University, Changsha 410083, China

Received 3 April 2025; accepted 18 August 2025

**Abstract:** To overcome reliance on molds and the difficulty of fabricating complex geometries with traditional C/C composites, direct ink writing (DIW) with UV/heat dual curing was employed to produce high-performance C/C composites. The rheological properties of the composite inks were systematically analyzed to assess the effects of phenolic resin (PR) and carbon fiber (CF) content. Results show pronounced shear-thinning behavior and strong thixotropy—both essential for stable DIW. Additionally, UV/heat curing behavior was characterized to provide theoretical insights for optimizing curing parameters. Notably, CF addition is found to significantly attenuate UV light penetration compared to pure PR. As CF content increases, the critical UV irradiation energy rises sharply from 68.47 to 911.19 mJ/cm$^2$, necessitating precise adjustments to curing parameters. Preforms were pyrolyzed in a carbon tube furnace to examine pore-formation characteristics, and chemical vapor infiltration (CVI) was applied to filling the resulting pores, yielding C/C composites with a flexural strength of 115.19 MPa.

**Key words:** C/C composites; dual curing; direct ink writing; rheology; curing behavior; chemical vapor infiltration

## 1 Introduction

Carbon fiber (CF) reinforced carbon composites (C/C composites) are widely used in aerospace, defense, and advanced industry for their outstanding mechanical properties, thermal resistance, and low density [1−3]. They are classified as continuous fiber reinforced composite (CFRC) or short/discontinuous fiber reinforced composite (SCFRC). Among them, CFRC is commonly prepared by unidirectional or multidirectional CF weave [4,5]. However, the complex braiding process and high costs restrict its use in manufacturing complex parts. To improve material efficiency and broaden applications, GUO et al [6] developed a molding route for high-performance SCFRC. However, expensive molds and difficulties in integral shaping of intricate parts remain [7].

Additive manufacturing (AM) is rapidly expanding into complex, high-performance applications driven by demands for autonomous design, flexible production, and novel materials. AM can markedly reduce cost, shorten lead times, and enable highly customized geometries [8]. Nevertheless, AM technologies for C/C composites remain largely exploratory [9]. Selective laser sintering (SLS) is a widely adopted process for C/C, C/SiC, and related systems [10,11]. YI et al [9] combined SLS with chemical vapor deposition (CVD) densification to obtain C/C composites (60 wt.% CF) with a flexural strength of approximately100 MPa. XU et al [12] used SLS to shape epoxy/SiC powder blends, with epoxy acting as a sacrificial binder; after debinding and

**Corresponding author:** Feng-ze JIANG, Tel: +86-15580970113, E-mail: fz.jiang@csu.edu.cn
https://doi.org/10.1016/S1003-6326(25)66866-X

polycarbosilane infiltration–pyrolysis, the C/SiC composites retained 220 MPa at room temperature and 203.7 MPa at 1600 °C. Building on these findings, CHEN et al [13] introduced a mechanically milled CF/phenolic resin (PR) feedstock for SLS. Printed CF/PR parts were debound to yield C/C preforms, which were then converted into dense C/SiC composites via reactive melt infiltration (RMI). Despite these advances, SLS offers limited control over CF orientation, resulting in random in-plane fiber distribution and low preform density.

Direct ink writing (DIW) has emerged as a powerful AM because it can orient CF during extrusion, thereby reinforcing composites [14,15]. The method is compatible with diverse material systems—water-based [16], liquid-resin [17], and solvent/polymer hybrids alike. In liquid-resin systems, preceramic polymers such as polysilazane [18], polycarbosilane [19], and poly(methyl-silsesquioxane) [20] are routinely used to fabricate SiC composites. FRANCHIN et al [17] demonstrated that shear at the nozzle tip aligns short carbon fibers with the extrusion direction when ceramic prepolymers are employed. WANG et al [21] printed complex C/SiC preforms by extrusion-based AM and systematically studied the influence of process parameters on structural stability, underscoring DIW's potential for intricate preform architectures. Moreover, fiber orientation, and thus mechanical, thermal, and electrical performance, can be tailored by tuning DIW parameters [22]. XIA et al [23] fabricated highly oriented core–shell C/SiC composites with a flexural strength of approximately 125 MPa, while CLARKSON et al [24] optimized a PR/CF ink to print complex C/C parts achieving 71.42 MPa. Despite these advances, the cited works rely solely on thermal curing, which limits the fabrication of hollow, truss, or other suspended structures.

In summary, this study employs dual curing via UV and heat in the DIW. During printing, UV curing pre-cures the printed structures, providing sufficient support strength and laying the foundation for constructing suspended geometries. The relationship between the rheological properties of composite inks and their material composition was investigated, and the mechanisms by which PR and CF content regulate these properties were explored. Furthermore, the UV and thermal curing behaviors of the composite inks were analyzed to optimize the curing process for producing high-performance printed samples. The effects of PR and CF content on the pore characteristics of the preforms were also studied. Chemical vapor infiltration (CVI) was subsequently employed to densify the preforms, resulting in high-performance C/C composites. This approach provides critical insights into composite ink formulation and establishes an effective strategy for fabricating high-performance C/C composites.

## 2 Experimental

Bisphenol A acrylate epoxy (EA) was purchased from Guangdong Wengjiang Chemical Reagent Co., Ltd. (Guangdong, China). PR, 1,6-hexamethylene diacrylate (HDDA), diphenyl (2,4,6-trimethylbenzoyl) phosphine oxide (TPO), phenylbis (2,4,6-trimethylbenzoyl) phosphine oxide (819), and benzenesulfonic chloride ($C_6H_5ClO_2S$) were purchased from Hunan, China. Specifically, the phenolic resin used was in liquid form, with a solid content of 79.8%−80.0% and a viscosity of 1450−1700 mPa·s at room temperature (25 °C). Fumed silica (FS, Aerosil 200) was purchased from Evonik Specialty Chemicals (Shanghai) Co., Ltd. (Shanghai, China). CF was sourced from Toray Co., Ltd. (Tokyo, Japan). Fiber lengths were measured by dispersing the fibers in alcohol, followed by observation and counting under an optical microscope. The average length was calculated based on measurements of more than 1000 individual CF, with the results presented in Fig. 1. The physical properties of the CF used in this study are summarized in Table 1.

The composite-ink preparation workflow is outlined in Fig. 2. First, EA and HDDA were blended at a 7∶3 mass ratio to tune viscosity. Next, 2.00 wt.% of a mixed photoinitiator (1.50 wt.% TPO + 0.50 wt.% 819) was incorporated and homogenized in a planetary mixer (TM−310, Smida, China) to yield a UV-curable resin with high curing depth (the curing-depth measurement procedure is illustrated in Fig. S1, and the corresponding optimization results are presented in Fig. S2 in Supplementary Materials). Prior to using the PR, 0.80 wt.% of the thermal curing agent $C_6H_5ClO_2S$ was added to adjust its initial curing temperature. The UV curable resin and PR were then mixed in

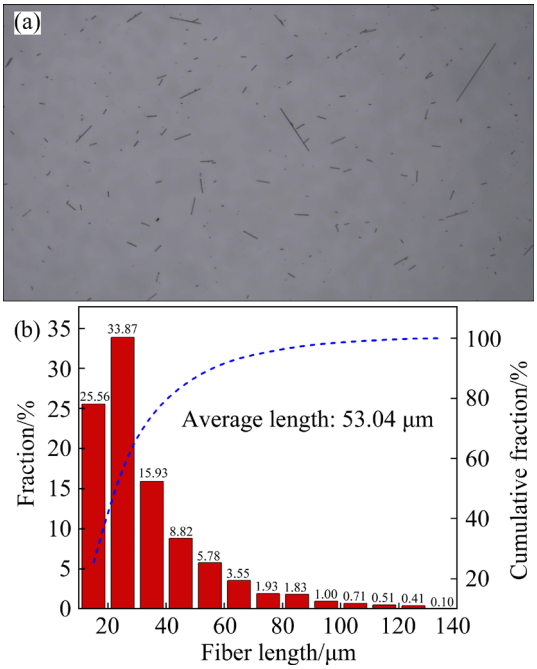


**Fig. 1** Microstructure (a) and fiber length distribution (b) of individual CF

**Table 1** Physical properties of CF adopted in this study

| Parameter | Value |
|---|---|
| Diameter/μm | 6.80–7.20 |
| Length/μm | ~53.04 |
| Density/(g·cm$^{-3}$) | 1.76–1.78 |

certain ratios, to which CF and FS were added. The composite inks were thoroughly blended using a planetary mixer to ensure uniform distribution of the components. The prepared composite inks were used on the same day for sample preparation, with the component ratios provided in Table 2.

**Table 2** Dual-cure ink composition (wt.%)

| Dual-cure ink | UV curable resin | PR | CF | FS |
|---|---|---|---|---|
| 5E5P | 48.5 | 48.5 | 0 | 3 |
| 4E6P | 38.8 | 58.2 | 0 | 3 |
| 3E7P | 29.1 | 67.9 | 0 | 3 |
| 4E6P5CF | 36.8 | 55.2 | 5 | 3 |
| 4E6P10CF | 34.8 | 52.2 | 10 | 3 |
| 4E6P15CF | 32.8 | 49.2 | 15 | 3 |

Research confirms a quantitative conversion between the mass fraction ($w_{CF}$) and volume fraction ($\varphi_{CF}$) of CF, expressed as

$$\varphi_{CF}=\frac{w_{CF}/\rho_{CF}}{w_{CF}/\rho_{CF}+w_m/\rho_m}\times 100\% \quad (1)$$

$$w_m=100\%-w_{CF} \quad (2)$$

where $w_m$ is the mass fraction of the matrix resin; $\rho_{CF}$ and $\rho_m$ represent the densities of the CF and matrix resin, respectively. The corresponding mass and volume fractions of CF are summarized in Table 3.

The molding schematic of the printed component is illustrated in Fig. 3. The composite inks were preformed through UV curing using an

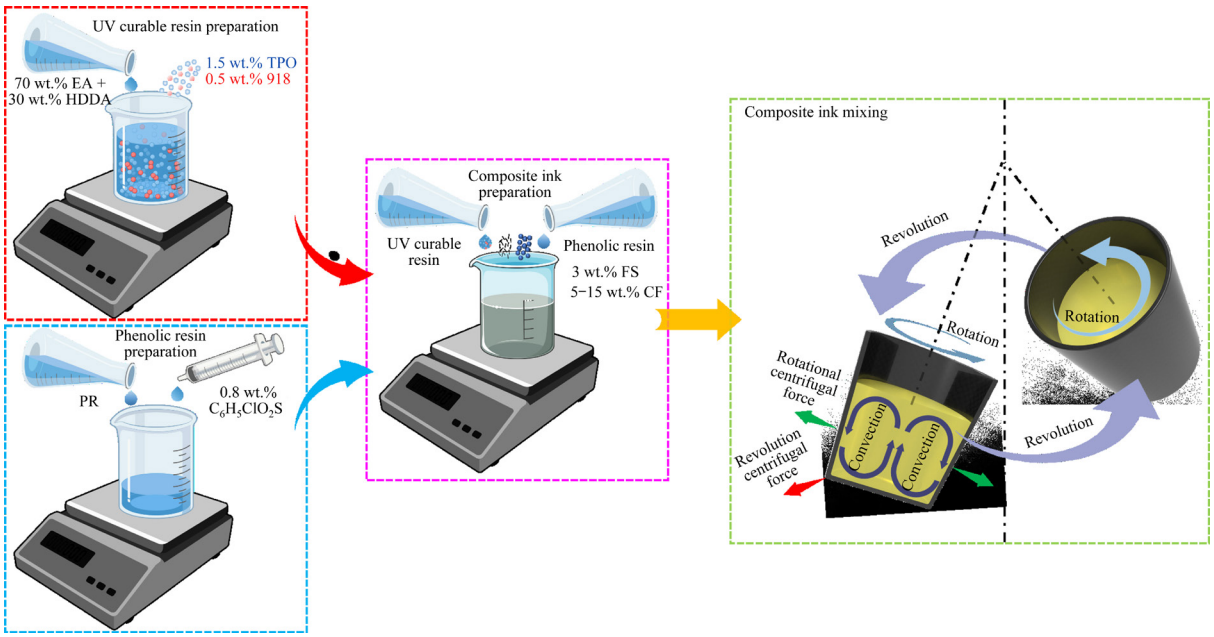


**Fig. 2** Schematic illustration of preparation process for dual-cure ink

**Table 3** Conversion of mass fraction to volume fraction for CF (%)

| Ink | Mass fraction | Volume fraction |
|---|---|---|
| 4E6P5CF | 5.00 | 3.78 |
| 4E6P10CF | 10.00 | 7.62 |
| 4E6P15CF | 15.00 | 11.63 |

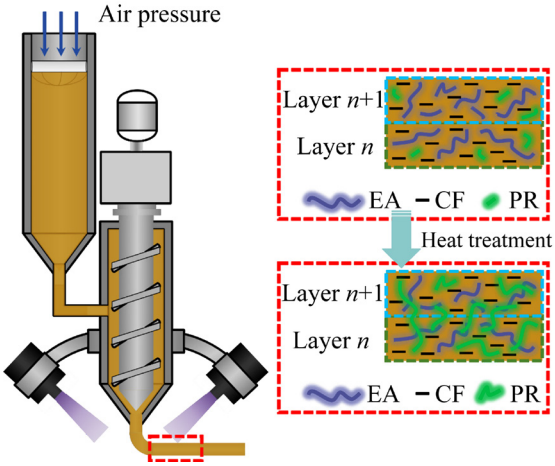


**Fig. 3** Schematic illustration of printing process for samples

independently built screw-extruder UV-assisted DIW. At this stage, the mechanical properties of the printed samples are weak, serving only a supporting role. Subsequently, the printed samples were transferred to a drying oven for heat curing to fully cure the incompletely cured portions, thereby enhancing their mechanical properties. To ensure effective molding of composite inks with different formulations, the relevant dual-curing parameters are summarized in Table 4 (The optimization of curing parameters is shown in Fig. S3 in Supplementary Materials).

To investigate the effect of the rheological properties of composite inks on printability, the rheological properties were tested using a rotational rheometer (DHR−2, TA Instruments, USA). A roughened parallel plate with a diameter of 20 mm was used, the test gap was set to be 1000 μm, and all tests were conducted at room temperature.

To investigate the thermal curing behavior of the composite inks and UV-cured samples, the enthalpy change during curing was analyzed using a differential scanning calorimeter (DSC 3500, Netzsch, Germany). The composite inks and UV-cured samples were gradually heated from room temperature under a nitrogen atmosphere at a rate

**Table 4** Dual-curing parameters for composite ink

| Parameter | Value |
|---|---|
| Nozzle diameter/mm | 1.0 |
| Layer thickness/mm | 0.4 |
| UV intensity/(mW·cm$^{-2}$) | 10−50 (without CF);<br>180−220 (with CF) |
| Printing speed/(mm·s$^{-1}$) | 20 |
| Infill density/% | 100 |
| Raster angle/(°) | 90 |
| Heat treatment | Non-vacuum: (80 °C, 2 h)+<br>(90 °C, 1 h)+(100 °C, 2 h)<br>Vacuum: (100 °C, 2 h)+<br>(120 °C, 1 h)+(140 °C, 2 h) |

of 10 °C/min up to 400 °C. After curing, the samples were removed to the carbon tube furnace for pyrolysis. The fully cured samples were post-cured at 250 °C for 2 h, then heated to a final pyrolysis temperature of 1600 °C at a heating rate of 5 °C/min and held for 2 h. The pyrolysis process was conducted under an argon atmosphere.

The carbon yield ($Y$) is measured as the ratio of the final mass after pyrolysis to the initial mass, and the formula is as follows:

$$Y=\frac{m_{\text{cured}}}{m_{\text{pyro}}}\times 100\% \tag{3}$$

where $m_{\text{cured}}$ is the initial mass of the printed samples before pyrolysis, and $m_{\text{pyro}}$ represents the final mass of the printed sample after pyrolysis.

According to the ASTM C372 — 20, the density ($\rho$) and apparent porosity ($P$) of the printed samples after full curing, pyrolysis, and densification by CVI were tested to analyze the print quality and porosity characteristics. The calculation formula is as follows:

$$\rho=\frac{m_{\text{d}}\cdot\rho_{\text{alcohol}}}{m_{\text{s}}-m_{\text{ss}}} \tag{4}$$

$$P=\frac{m_{\text{s}}-m_{\text{d}}}{m_{\text{s}}-m_{\text{ss}}}\times 100\% \tag{5}$$

where $m_{\text{s}}$ is the saturated mass, $m_{\text{d}}$ represents the dry mass, and $m_{\text{ss}}$ denotes the submerged mass. The density of alcohol ($\rho_{\text{alcohol}}$) at room temperature is 0.7893 g/cm³.

Linear shrinkage ($S$) was calculated by comparing the dimensional changes in length, width, and thickness of the printed samples before and

after pyrolysis using Eq. (6), averaging at least five measurements to minimize errors:

$$S=\frac{x_{\text{cured}}-x_{\text{pyro}}}{x_{\text{cured}}}\times 100\% \quad (6)$$

where $x_{\text{cured}}$ is the dimensions of the printed samples before pyrolysis, including length ($L$), width ($W$), and thickness ($T$), and $x_{\text{pyro}}$ represents the dimensions of the printed samples after pyrolysis.

In this study, the printed samples were prepared using UV-assisted DIW combined with UV/thermal dual curing, as shown in Fig. 4(b). The shape and size of the test samples conform to ASTM 7264/7264M standards, and the dimensions and print paths are shown in Fig. 4(a). The flexural strength of the C/C composites was measured using a universal testing machine (UTM4204, Suns, China) at a rate of 0.5 mm/min. To minimize experimental errors and ensure accuracy, at least five samples were prepared for each test. The flexural strength of C/C composites was calculated using Eq. (7):

$$\sigma_{\text{flexure}}=\frac{3F\dot{L}}{4\bar{b}\bar{d}^{2}} \quad (7)$$

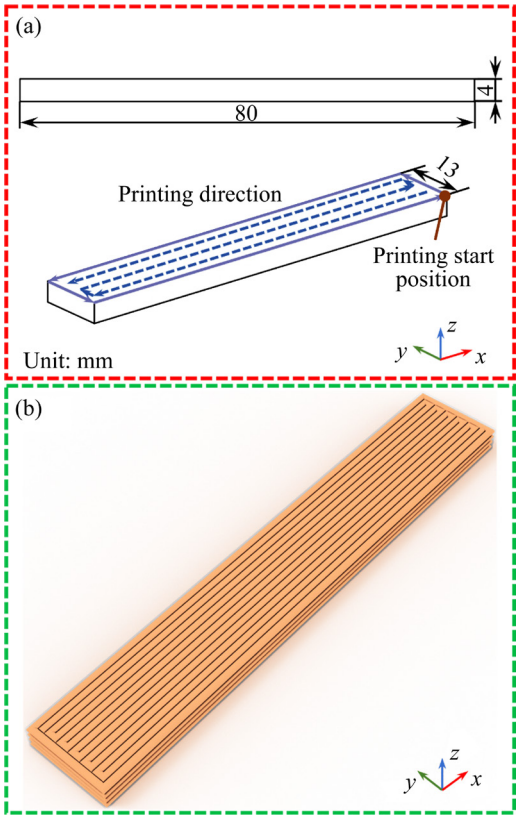


**Fig. 4** Schematics of flexural sample for present study: (a) Dimensions; (b) Printing flexural sample

where $F$ is the maximum load, $\dot{L}$ represents the outer span length, set to be $16T$, $\bar{b}$ denotes the average width, and $\bar{d}$ is the average thickness.

To understand the distribution of fillers within the matrix and the interlayer interfacial bonding in the printed samples, the surface morphology of the cross-section was analyzed using scanning electron microscopy (SEM, MIRA4, Tescan, The Czech Republic). The C/C composite preforms and its pore characteristics after densification were also investigated to assess the densification effect and the failure mechanism.

## 3 Result and discussion

### 3.1 Rheology and printability

Composite inks are often designed to exhibit shear-thinning behavior, which allow for low viscosity at high shear rates, ensuring smooth extrusion from the nozzle. At the same time, the inks must be sufficiently resistant to flow to prevent the printed samples from collapsing under static conditions. For this reason, the rheological properties of the composite inks were characterized in detail, as shown in Fig. 5. Figure 5(a) shows the variation of viscosity with shear rate for the composite inks, from which it can be observed that all composite inks exhibit shear-thinning behavior. Since the viscosity of PR is higher than that of UV-cured resin, the viscosity of the composite inks increases as the PR content rises. Additionally, the inclusion of CF increases the solid content of the composite inks, further elevating the viscosity. The relationship between shear stress, and storage modulus and loss modulus of the composite ink is analyzed through a stress amplitude experiment, as shown in Fig. 5(b). This includes the equilibrium storage modulus ($G'_0$) and yield shear stress ($\tau_y$) of the composite ink, as shown in Fig. 5(c). A higher $\tau_y$ means that the lower layers of the printed samples are less likely to collapse under the weight of the upper layers [25]. At the same time, a larger $G'_0$ helps the composite inks maintain their shape when building tall structures [26] and prevents sagging when constructing spanning features [27]. As shown in Fig. 5(b), at low shear stresses, $G'$ of the composite inks is greater than $G''$, indicating that, at this point, the inks exhibit more solid-like behavior than viscous behavior. As the shear stress

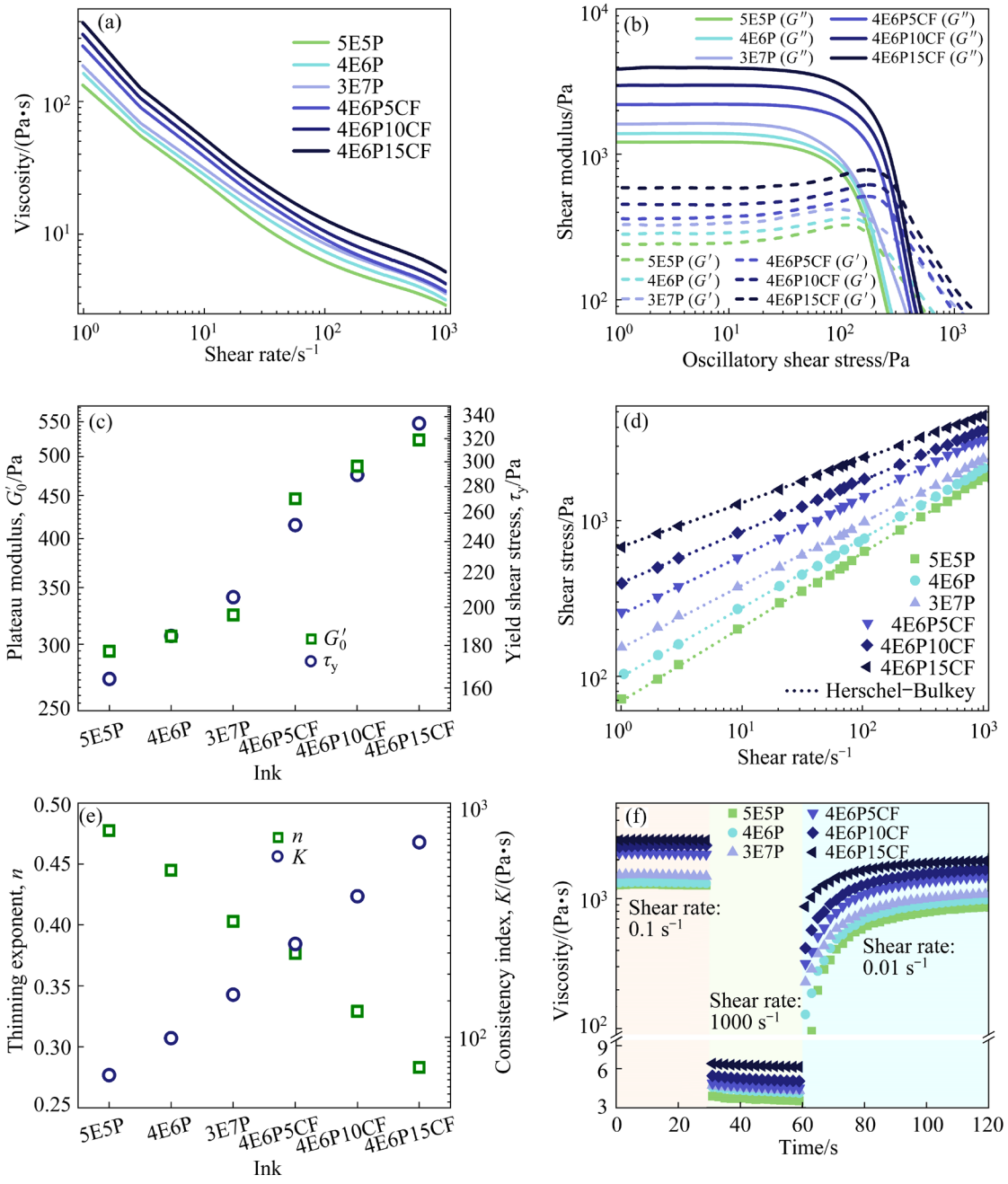


**Fig. 5** Rheological behavior of composite ink: (a) Viscosity versus shear rate; (b) Shear modulus, $G'$ and $G''$, versus oscillatory shear stress; (c) $G_0'$ and $\tau_y$ of different composite inks; (d) Shear stress of composite inks; (e) $K$ and $n$ of different composite inks; (f) Thixotropic behavior of composite ink

increases and surpasses the yield shear stress $\tau_y$ of the composite inks, $G''$ will exceed $G'$, at which point the ink will shift to more viscous behavior and exhibit improved fluidity. To further investigate the correlation between shear stress and shear rate (Fig. 5(d)), the Herschel−Bulkley power-law model is employed [28]:

$$\tau=\tau_y+K\gamma^n \tag{8}$$

where $\tau$ is the shear stress, $K$ is the consistency index, $\gamma$ is the shear rate, and $n$ is the flow behavior index.

Figure 5(d) clearly demonstrates that the Herschel−Bulkley power-law model accurately fits the experimental data, with $R^2_{adj}$>0.99. Figure 5(e) further illustrates the key parameters of these fitted models. The results show that the $n$ value for the composite inks is less than 1 across the range of shear rates studied, indicating that all inks exhibit shear-thinning behavior [29]. The shear-thinning

behavior becomes more pronounced with the addition of PR and CF, further confirming the accuracy of the results shown in Fig. 5(a). In addition, the $K$ increases significantly with the addition of PR and CF, rising from 68.96 to 679.31 Pa·s. This increase is particularly notable after the addition of CF (e.g., 4E6P and 4E6P5CF), indicating the formation of a crosslinked network between the resin molecular chains and the CF. This also suggests that the viscosity of the composite inks is increased, making the flow behavior more dependent on the applied shear stress. Specifically, the inks do not flow under low shear stress, a characteristic that is beneficial for the DIW of composite inks [24].

Thixotropic properties describe the ability of composite inks to return to a state close to their original form after the removal of shear stress. As thixotropic properties are enhanced, the stability of the printed sample after extrusion from the nozzle and its ability to maintain precise geometry are significantly improved [30]. As shown in Fig. 5(f), with the addition of FS to the composite inks, the inks are able to rapidly transition from a low-viscosity state to a high-viscosity state when the shear rate is abruptly reduced. This behavior helps maintain the shape of the printed sample during printing, as illustrated in Fig. 6(a) [31]. In addition, FS forms weak hydrogen bonds between the polymer molecular chains and the fillers, effectively preventing the precipitation and agglomeration of the fillers, as shown in Figs. 6(b, c), where the sample is left to stand for 2 h.

### 3.2 UV curing performance of composite ink

Figures 7(a, b) illustrate the relationship between the curing depth $C_d$ (test method shown in Fig. S3 in Supplementary Materials) and the UV exposure energy ($E$) of the composite inks at different PR and CF contents. Figure 7(a) shows that the $C_d$ of the composite inks gradually decreases as the PR content increases. Specifically, $C_d$ decreases from 0.74 to 0.51 mm when the $E$ is approximately 300.00 mJ/cm². Figure 7(b) illustrates the effect of CF content on the UV curing behavior of composite inks. It is evident that the addition of CF significantly alters the $C_d$ of composite inks. When the $C_d$ is 0.20 mm, the $E$ required for 4E6P is 121.89 mJ/cm², whereas 4E6P5CF requires 1825.40 mJ/cm², showing a significant increase in the required UV exposure energy. Additionally, the $C_d$ of the composite inks decreases further from 0.21 to 0.09 mm with an increase in CF content.

The Jacob's equation [29] was used to explore the reasons for these changes in UV curing behavior, as follows:

$$C_d = D_p \ln\frac{E}{E_c} = D_p\left(\ln E - \ln E_c\right) \tag{9}$$

where $D_p$ represents the penetration depth coefficient (mm), which describes the depth at which the $E$ decays to 1/e in the composite inks, indicating the sensitivity of the inks to $E$; $E_c$ is the critical curing energy (mJ/cm²), which represents the minimum energy required to initiate the polymerization.

$D_p$ and $E_c$ can be obtained from the linear fitting of $C_d$–ln $E$, as shown in Figs. 7(c, d). The increase in both PR and CF content leads to a decrease in $D_p$, indicating that the addition of PR and CF enhances the dissipation of $E$ in the composite inks and hinders the absorption of UV by the deeper photoinitiators, thereby reducing the curing depth [32]. In addition, $E_c$ of the composite inks increases with the rising content of PR and CF, particularly with the addition of CF, which causes a rapid increase in $E_c$ from 68.47 to 911.19 mJ/cm². This phenomenon suggests that both PR and CF

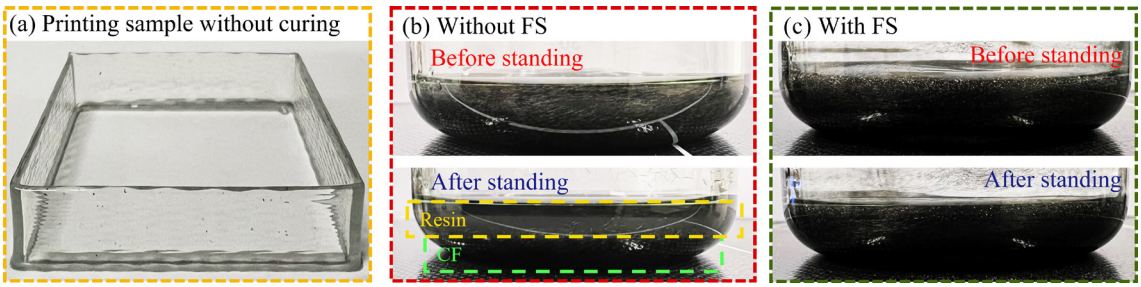


**Fig. 6** (a) Printing sample (50 mm × 50 mm × 8 mm) without curing; (b) Composite inks without FS; (c) Composite inks with FS

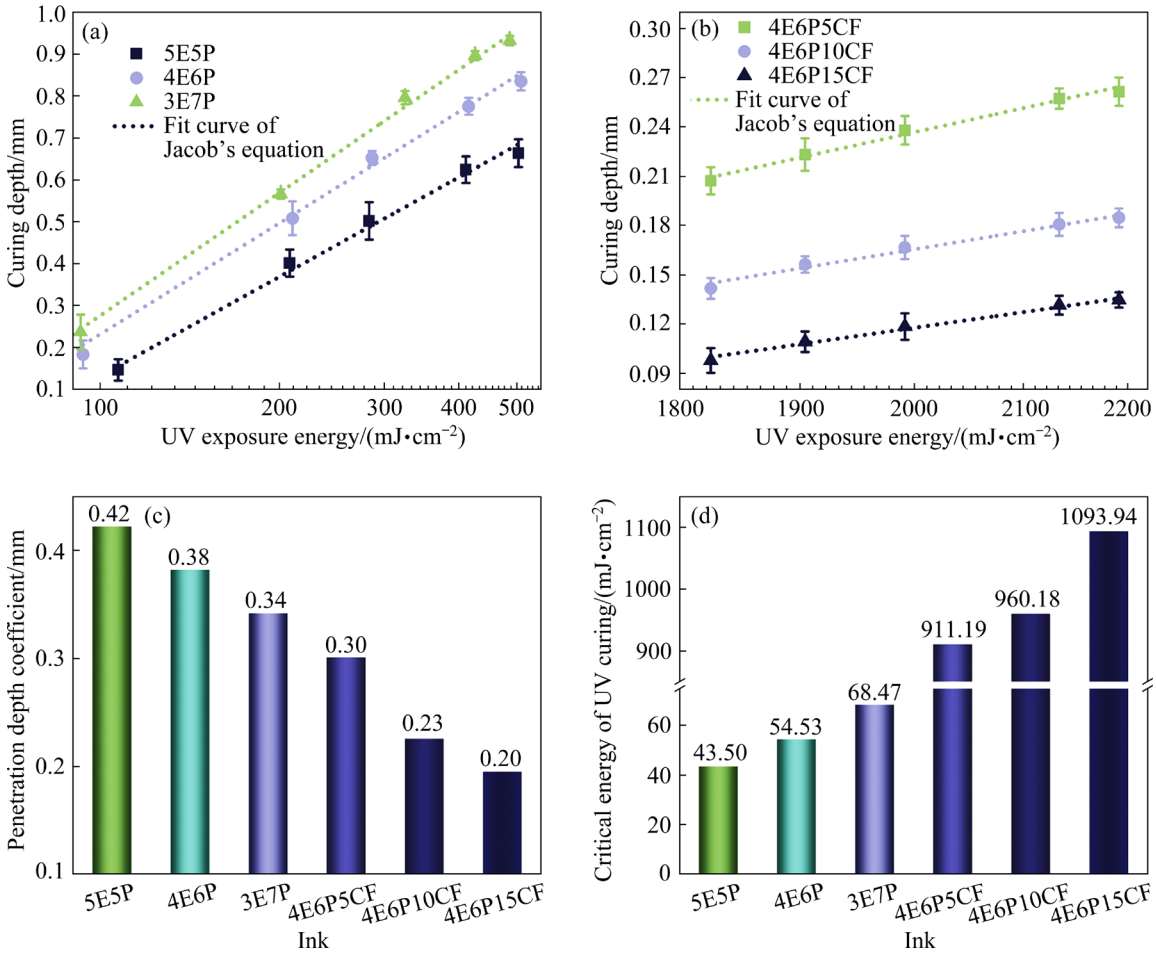


**Fig. 7** UV curing performance of composite ink: (a) Curing depth ($C_d$) without CF; (b) Curing depth ($C_d$) with CF; (c) Penetration depth coefficient ($D_p$); (d) Critical curing energy ($E_c$)

block the incident UV [33], and CF absorbs part of the energy, reducing the amount of UV that penetrates the matrix of the composite inks and triggers the photopolymerization. As a result, this manifests as an increase in the $E$ required for curing.

### 3.3 Thermal curing behavior

By analyzing the enthalpy change during the curing of composite inks (Fig. 8), the thermal curing behavior was explored to provide a theoretical basis for optimizing the thermal curing parameters. As shown in Fig. 8(a), the initial curing temperature of the UV-cured resin is approximately 182 °C, and its curing process exhibits two endothermic peaks, with peak temperatures of 255 and 323 °C, respectively. This is attributed to the presence of two types of oligomers in the UV-cured resin, namely, EA and HDDA. With the addition of PR, the endothermic peak during the curing of the UV-cured resin shifts to a lower temperature, and the initial curing temperature is reduced to approximately 103 °C. This indicates that the heat released from the PR during curing promotes the thermal curing of the UV-cured resin. It is well known that the curing of PR involves condensation polymerization, which generates water that can lead to defects in the printed samples. To prevent an overly rapid reaction, $C_6H_5ClO_2S$ was introduced to lower the initial curing temperature of the composite inks, allowing for slower curing at lower temperatures. Additionally, a vacuum environment was used to effectively remove the water generated during the reaction, thereby preventing defects inside the printed samples. Figure 8(a) also shows that the addition of 0.8 wt.% $C_6H_5ClO_2S$ reduces the initial curing temperature of the composite inks from 101.03 to 80.86 °C, providing theoretical support for optimizing the thermal curing process. Figures 8(b, c) show the endothermic peaks of the composite inks and the UV-cured printed samples during curing. Since the UV-cured resin has been

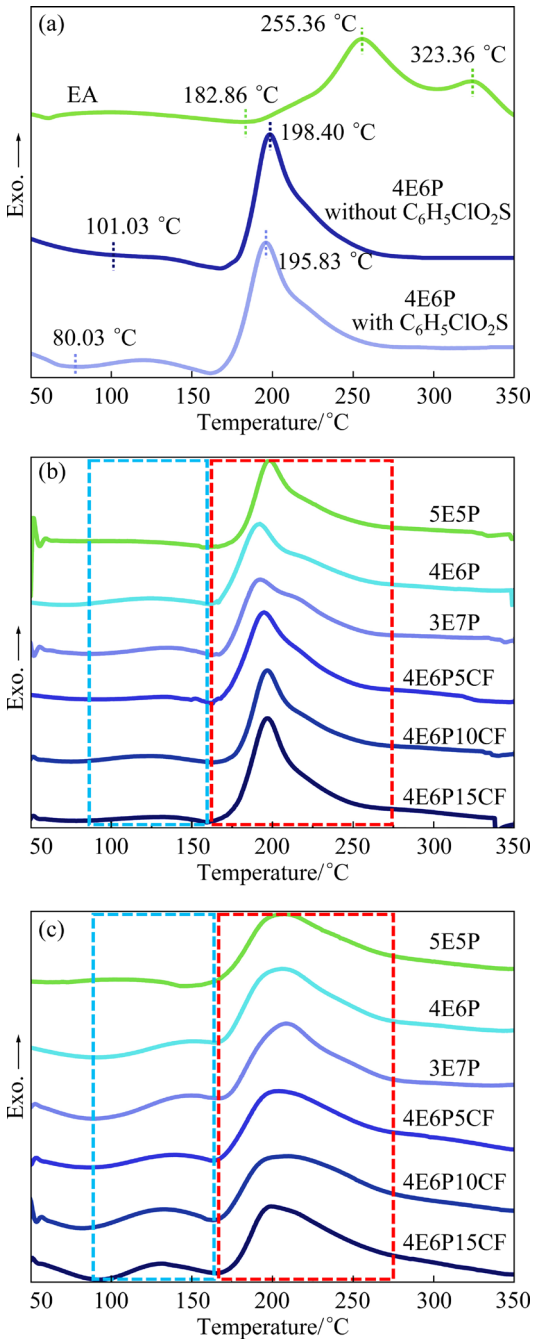


**Fig. 8** Thermal curing behavior of composite ink: (a) Effect of PR and $C_6H_5ClO_2S$ on thermal curing behavior; (b) DSC curves of composite ink; (c) DSC curves of UV-cured sample

partially cured by the UV-assisted DIW, its main endothermic peak (marked in red) becomes flatter. Meanwhile, as the content of PR and CF increases, the secondary endothermic peak (labeled in blue) becomes more pronounced. This is because the addition of PR and CF hinders the UV curing of some UV-cured resin, causing these resins to rely on the heat released during the curing of PR for further curing, regulating the content of PR and CF, enabling the preparation of hollow, truss, and other structures.

### 3.4 Influence of PR and CF content on printing quality

To thoroughly analyze the printing quality of the printed samples, the density and apparent porosity were theoretically calculated using the Archimedes method. Additionally, micro-morphological observations of their cross-sections were conducted to assess the bonding at the inter-layer interfaces and identify defects such as internal pores. Figure 9(a) compares the densities of the printed samples with varying PR and CF content. It can be observed that the density of the printed samples increases slightly with the rise in PR and CF content. The primary reason for this increase in density is that the densities of PR and CF are higher than that of EA. As shown in Fig. 9(b),

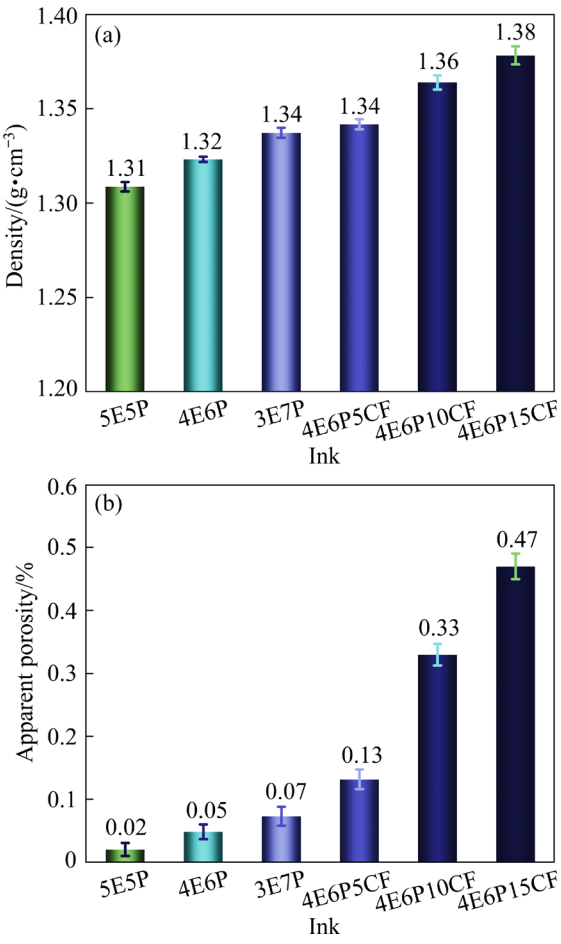


**Fig. 9** (a) Density of printed samples; (b) Apparent porosity of printed samples

the apparent porosity of the printed samples increases slightly from 0.02% to 0.47% with the rise in PR and CF content. However, the measured apparent porosity remains relatively low, indicating that the printed samples possess good printing quality and are overall dense.

Figures 10(a−i) illustrate the bonding and pore characteristics at the interfaces within the printed samples. As seen in Figs. 10(a−f), although the increase in PR and CF content raises the viscosity of the composite inks (Figs. 5(a, f)), which hinders molecular diffusion between layers and reduces interlayer bonding, no obvious delamination is observed in the cross-sections. This suggests good adhesion between the layers. The strong adhesion can be attributed to the heat curing that the printed samples undergo after UV curing. During this process, the incompletely cured PR is gradually cured, promoting interlayer adhesion and enhancing the interlayer bonding in the printed samples. The distribution and surface condition of CF within the printed samples were also analyzed, as shown in Figs. 10(g−i). SEM images reveal that even with a CF content of 15.00 wt.%, the CF is uniformly distributed in the matrix without noticeable agglomeration. Additionally, pores (marked in blue) resulting from the pull-out of CF are visible, highlighting the bonding between the CF and the matrix, as shown in Figs. 10(g−i). It can be observed that the surface of the CF is partially encapsulated by the resin, indicating effective bonding between the CF and matrix. This bonding facilitates the efficient transfer of load from the matrix, which has relatively lower mechanical

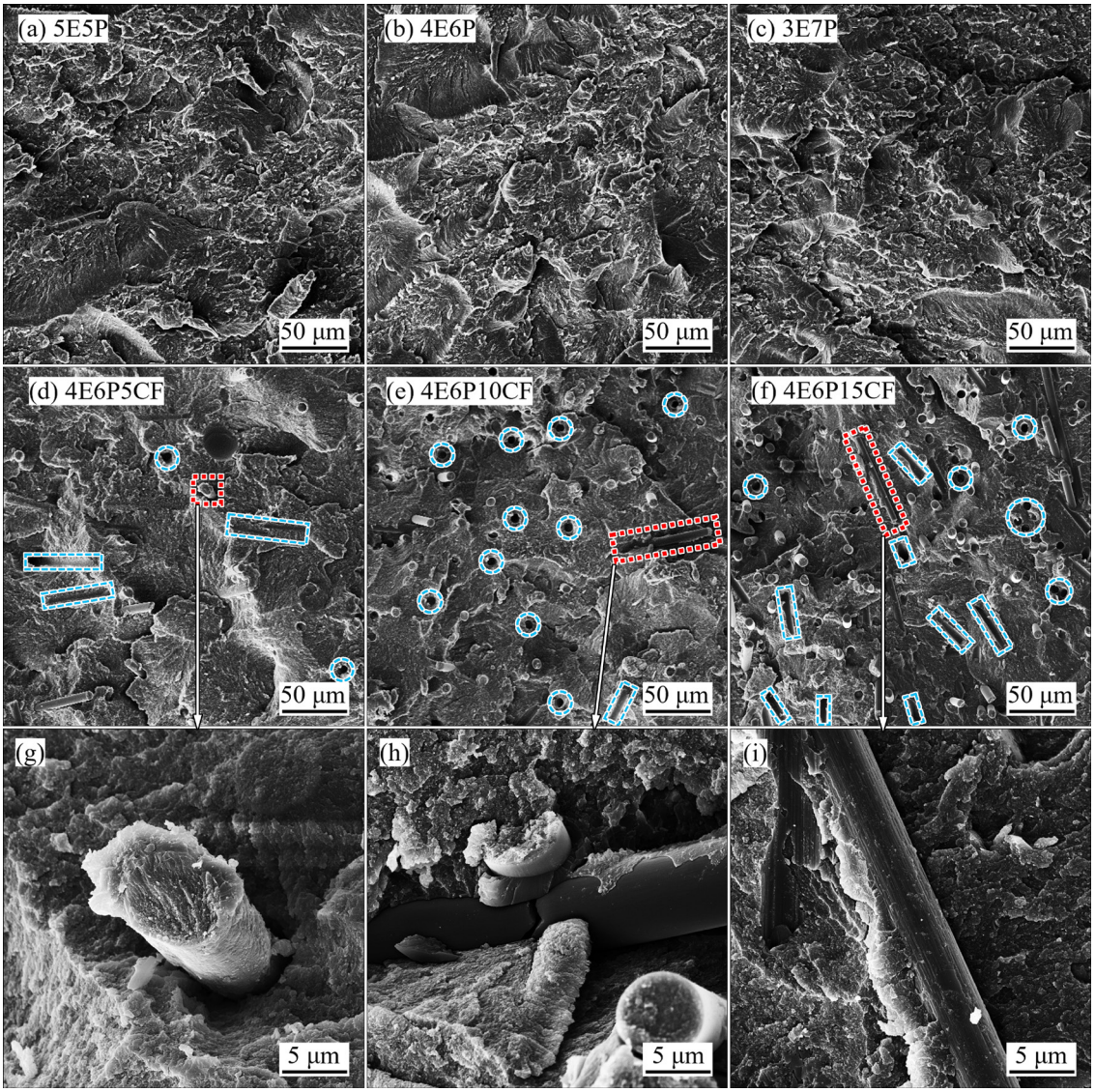


**Fig. 10** (a−c) Section morphology of printed samples without CF; (d−f) Section morphology of printed samples with CF; (g−i) CF morphology in matrix

strength, compared to the CF, which possess higher mechanical strength. Consequently, this enhances the mechanical properties of the printed samples when subjected to external loads.

### 3.5 Physical and apparent porosity characteristics

Figure 11 presents the physical properties of the printed samples after pyrolysis, including carbon yield, density, apparent porosity, and linear shrinkage. Generally, the carbon yield of PR ranges from 57% to 65%, whereas UV-cured resins typically exhibit a carbon yield of approximately 10%. As shown in Fig. 11(a), the carbon yield of the printed samples increases from 34.46% to 45.37% with higher PR content. Additionally, the carbon yield rises from 40.72% to 49.45% as CF content

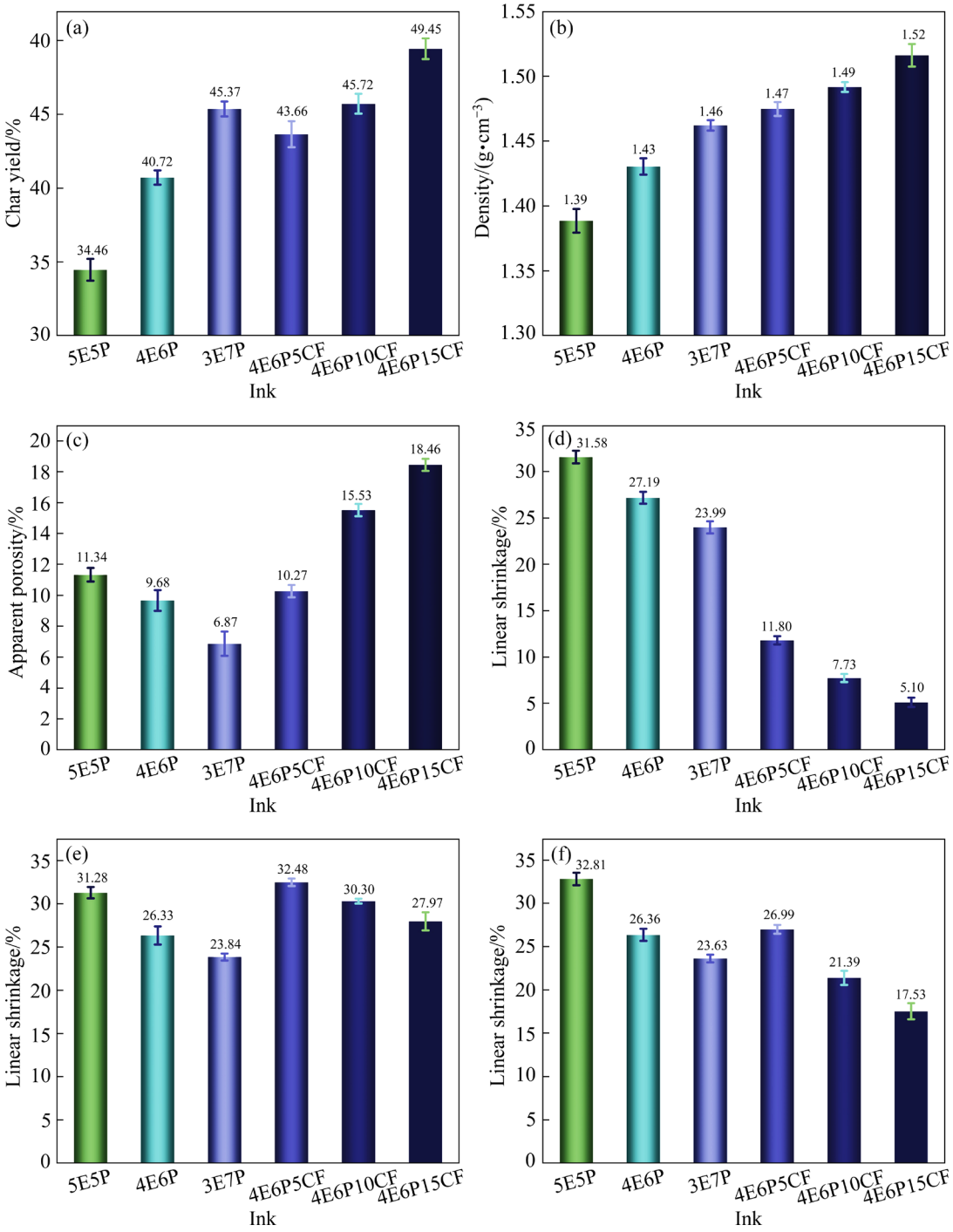


**Fig. 11** Physical properties of printed samples after pyrolysis: (a) Char yield; (b) Density; (c) Apparent porosity; (d) Linear shrinkage in length direction; (e) Linear shrinkage in width direction; (f) Linear shrinkage in thickness direction

increases. This can be attributed to the fact that CF undergoes minimal loss during pyrolysis and retains its original structure in the C/C composite preforms. Figure 11(b) illustrates the density changes of the printed samples after pyrolysis. The density of the preforms increases with the rise in PR content, as PR with a high carbon yield contributes to the formation of a denser structure. Meanwhile, as shown in Fig. 11(c), apparent porosity decreases progressively from 11.34% to 6.87%, indicating that the pyrolyzed structure becomes denser. While the addition of CF helps to suppress shrinkage during pyrolysis, it also introduces additional pores, leading to an increase in apparent porosity from 9.68% to 18.46%. However, the higher density of CF compared to resin carbon results in a slight increase in the density of the preforms.

Figures 11(d−f) display the linear shrinkage of the preforms in the length (L), width (W), and thickness (T) directions. For samples without CF, shrinkage is relatively uniform across all three directions and decreases with increasing PR content. In samples containing CF, the linear shrinkage of 4E6P5CF, 4E6P10CF, and 4E6P15CF follows a similar trend. Notably, in the printing direction (length direction), the presence of rigid CF effectively suppresses shrinkage, reducing it significantly from 27.19% to 5.10%. In comparison to the L direction (aligned with the CF direction), C/C composite preforms demonstrate anisotropic shrinkage in the W and T directions. This anisotropy arises from the alignment of CF along the printing direction [34]. Furthermore, the stacking of CF in the W and T directions contributes to a gradual reduction in linear shrinkage along these dimensions.

To further analyze the internal pore characteristics of the C/C composite preforms, cross-sections were examined using SEM, as shown in Fig. 12. Figures 12(a−c) illustrate the internal pore characteristics of the printed samples without CF addition after pyrolysis. It is clearly observed that cracks, including transverse and longitudinal (highlighted in blue) cracks (for details on cross-section selection, refer to Fig. S4 in Supplementary Materials), are present. This also suggests that the printed samples exhibit good structural integrity. However, the internal cracks gradually decrease with the increasing PR content, which aligns with the apparent porosity trend shown in Fig. 12(c). This can be attributed to the fact that higher PR content enhances the carbon yield after pyrolysis, thereby reducing crack formation. A similar phenomenon is observed in preceramic polymer-based systems, where lower conversion during pyrolysis leads to increased crack formation [35,36]. Notably, the addition of CF results in a gradual reduction in longitudinal cracks, as shown in Figs. 12(d−f). Previous studies have demonstrated that incorporating fillers can significantly mitigate crack formation during high-temperature conversion [17,20]. In this study, FS and CF were used as fillers, and longitudinal cracks gradually decrease with increasing CF content. Additionally, the addition of CF significantly reduces UV curing of the composite inks, leading to the formation of a weak interface between the layers of the printed samples. This weak interface becomes the starting point for cracks to form during pyrolysis. Further observation of the matrix reveals that pores are formed around the oriented fibers during pyrolysis due to their restricted shrinkage, as shown in Figs. 12(g−i). Moreover, the number of pores increases significantly with rising CF content, which is one of the factors contributing to the increase in apparent porosity of the preforms.

### 3.6 Influence of apparent porosity characteristics on CVI

The densification of C/C composite preforms by CVI was employed to fill the pores generated during pyrolysis, thereby enhancing the mechanical properties of the C/C composites. Figures 13(a, b) show the density and apparent porosity of the C/C composites after densification. Compared to the undensified C/C composite preforms (Figs. 11(a, b)), the density gradually increases, while the apparent porosity decreases after densification. This indicates that during CVI, carbon atoms effectively adhere to the surface and internal pores of the preforms, progressively filling the pores and resulting in the densification of the C/C composites.

The flexural strength of the C/C composites was characterized, as shown in Fig. 13(c). It is evident that with an increase in PR content, the flexural strength of the C/C composites decreases

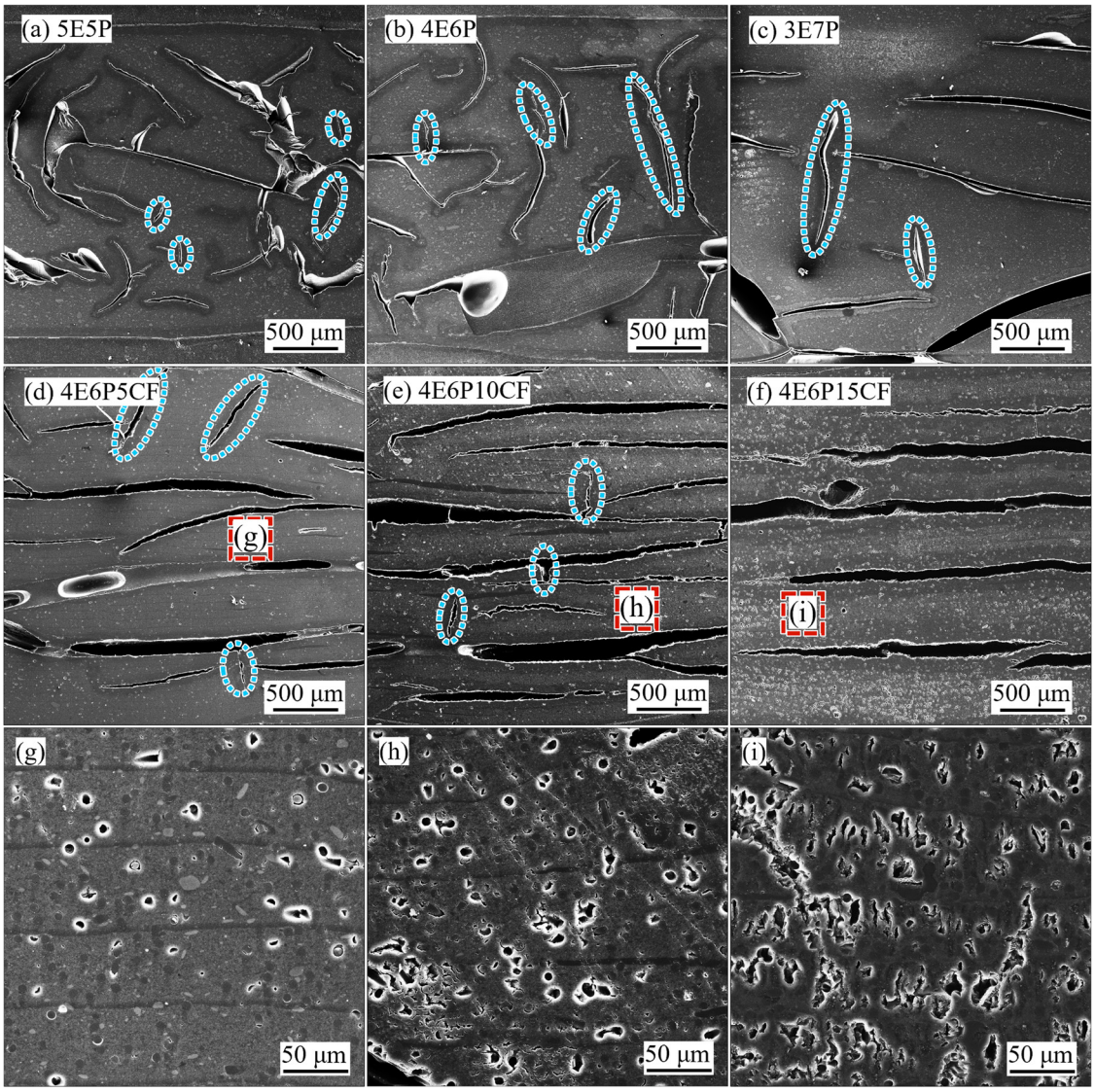


**Fig. 12** Section morphology of printed samples after pyrolysis: (a−c) Printed samples without CF; (d−f) Printed samples with CF; (g−i) Magnification showing additional features in cross-section

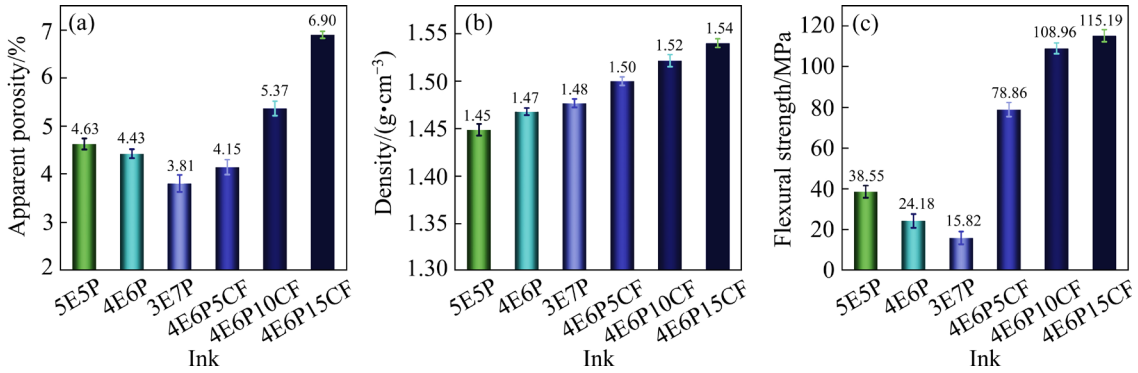


**Fig. 13** Physical and mechanical properties of C/C composites: (a) Apparent porosity; (b) Density; (c) Flexural strength

from 38.55 to 15.82 MPa, with a reduction of 58.62%. However, the flexural strength increases rapidly from 24.18 to 115.19 MPa with the addition of CF. To further analyze the mechanism behind the effect of CVI on the flexural strength of the C/C composites, the cross-sections of the composites were examined using scanning electron microscopy to evaluate the densification effect.

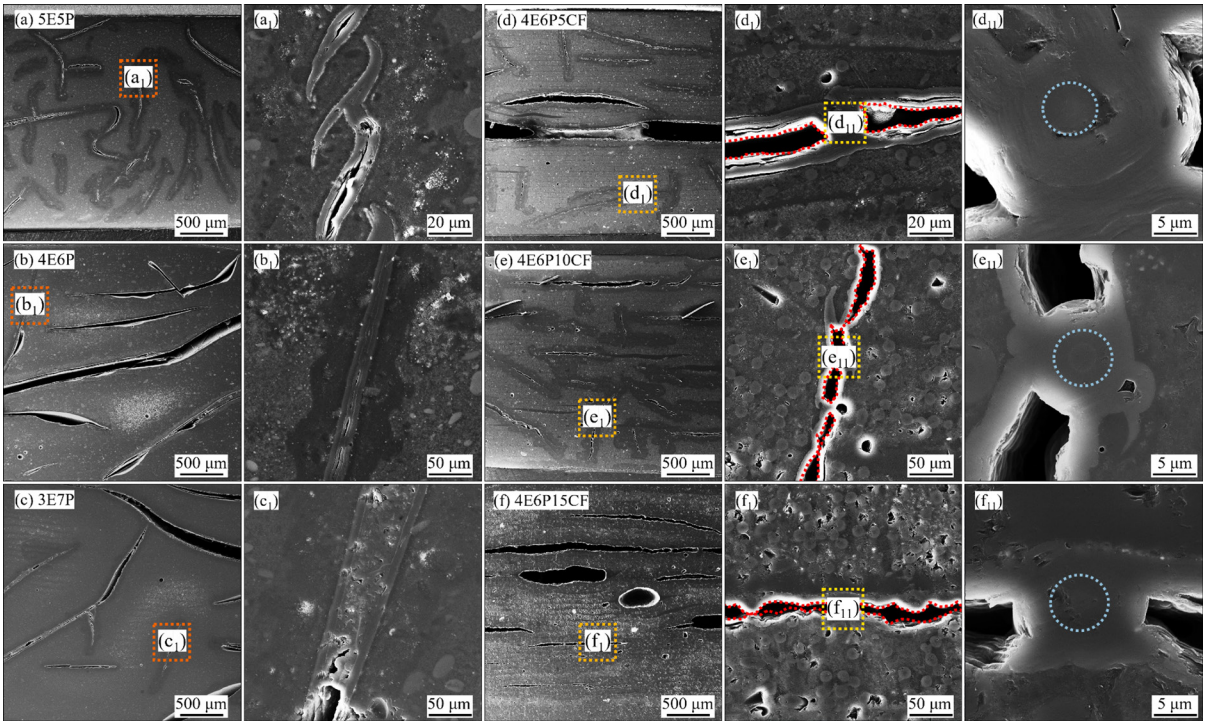


**Fig. 14** Section morphology of printed samples after CVI: (a−c) Printed samples without CF; (d−f) Printed samples with CF; ($a_1$−$f_1$, $d_{11}$−$f_{11}$) Magnification showing additional features in cross-section

Figure 14 illustrates the micro-morphology of the cross-section of the C/C composites. Figures 14(a−c) show that the filling effect of CVI on the pores diminishes significantly as the PR content increases, resulting in a higher number of residual pores within the C/C composites. This leads to a gradual decline in flexural strength. Further examination of the pore-filling process, as shown in Figs. 14($a_1$−$c_1$), reveals that during CVI, carbon atoms adhere to the pore walls, forming a deposition layer that thickens progressively to fill the pores through continuous deposition. However, the narrow ends of the pores are filled preferentially, converting initially open pores into closed ones. This transformation restricts further deposition, leaving some micropores unfilled within the matrix. This phenomenon explains the incomplete pore filling observed in 3E7P. With the addition of CF, as depicted in Figs. 14(d−f), the increased apparent porosity enhances the ability of the preforms to accommodate pore filling during CVI. Furthermore, since CF inhibits shrinkage during pyrolysis, more micropores are retained in the preforms (Figs. 12(g−i)). These micropores can also be effectively densified during CVI, as demonstrated in Figs. 14($d_1$−$f_1$). Figures 14($d_{11}$−$f_{11}$) show that CF exposed in the pores after pyrolysis develops a distinct deposition layer on its outer surfaces during CVI. This process gradually transforms interconnected large pores into isolated smaller pores (blue dotted line), limiting further pore filling. However, this also enables the C/C composites to efficiently transfer external forces to the CF, thereby improving their flexural strength, as illustrated in Fig. 13(c).

## 4 Conclusions

(1) The consistency index ($K$) rises from 68.96 to 679.31 Pa·s with increasing PR and CF content. The pronounced shear-thinning behavior lowers viscosity under stress, ensuring smooth extrusion and reliable DIW.

(2) The UV curing behavior of the composite inks is described by Jacob's equation. The observed decrease in $D_p$ indicates that PR and CF additions enhance UV dissipation within the ink matrix, consequently elevating the $E_c$ required for photopolymerization from 68.47 to 911.19 mJ/cm$^2$. This increase demonstrates significant UV absorption capacity of CF, which attenuates incident radiation and reduces effective curing

energy at the reaction front. Thermal curing behavior shows that the heat released by PR during the curing promotes the curing of UV-cured resin. Moreover, the incorporation of $C_6H_5ClO_2S$ lowers the initial curing temperature of the composite inks, providing a theoretical basis for optimizing thermal curing.

(3) Pyrolysis preserves CF orientation, shrinking along the fiber direction from 27.19% to 5.10%. Porosity simultaneously rises from 9.68% to 18.46% with higher CF content, facilitating subsequent CVI.

(4) During CVI, pyrolytic carbon deposits on exposed CF, converting large interconnected pores into smaller isolated ones while bridging pore walls. This microstructural evolution efficiently transfers external loads to the fibers, boosting flexural strength from 24.18 to 115.19 MPa.

## CRediT authorship contribution statement

**Xin YE:** Methodology, Formal analysis, Data curation, Writing − Original draft; **Qian LU:** Methodology, Formal analysis; **Lu-tong WU:** Conceptualization, Methodology; **Ming-liang XU:** Methodology, Investigation; **Xiang XIONG:** Methodology, Formal analysis; **Feng-ze JIANG:** Project administration, Writing − Review & editing, Resources.

## Declaration of competing interest

The authors declare that they have no known competing financial interests or personal relationships that could have appeared to influence the work reported in this paper.

## Acknowledgments

This research was supported by State Key Laboratory of Powder Metallurgy, Central South University, Changsha, China.

## Supplementary Materials

Supplementary Materials in this paper can be found at: http://tnmsc.csu.edu.cn/download/18-p3057-2025-0324-Supplementary_Materials.pdf.

## References

[1] GILLARD A P, COUÉGNAT G, CHUPIN S, VIGNOLES G L. Modeling of the non-linear mechanical and thermomechanical behavior of 3D carbon/carbon composites based on internal interfaces [J]. Carbon, 2019, 154: 178−191.

[2] GUO Fei, FEI Qing-guo, ZHANG Pei-wei, LI Yan-bin, WANG Meng, GUPTA N. Dynamic shear fracture behaviors and “pseudo-plastic” constitutive model of carbon/carbon composite pins [J]. International Journal of Mechanical Sciences, 2020, 187: 105903.

[3] FENG Wei, ZHANG Yan, LIU Lei, LI Bo-yan, ZHANG Jia-ping, CHEN Xi, HE Zi-bo, TANG Cheng-wei, ZHANG Hai-jun, HAN Qin-xin. High-frequent pulsing ablation of C/C−SiC−$ZrB_2$−ZrC composite for different cycles to 2000 times in plasma [J]. Transactions of Nonferrous Metals Society of China, 2023, 33(2): 553−562.

[4] RAN Li-ping, RAO Fei, PENG Ke, YIN Huan, YI Mao-zhong. Preparation and properties of C/C−$ZrB_2$−SiC composites by high-solid-loading slurry impregnation and polymer infiltration and pyrolysis (PIP) [J]. Transactions of Nonferrous Metals Society of China, 2019, 29(10): 2141−2150.

[5] PENG Zheng, MIAO Chun-mao, SUN Wei, XU Yong-long, CHEN Hai-kun, LIU Yu-feng, ZHANG Hong-bo, XIONG Xiang. High-temperature thermal stability of C/C−ZrC−SiC composites via region labeling method [J]. Transactions of Nonferrous Metals Society of China, 2022, 32(10): 3349−3361.

[6] GUO Ling-jun, LI He-jun, LI Ke-zhi. Effect of surface treatments of short carbon fibers on the properties of pitch-based C/C composites [J]. Carbon, 2009, 47(8): 2146.

[7] WANG Wen-qing, ZHANG Lu, DONG Xing-jie, WU Jian-qin, ZHOU Qing, LI Su-wen, SHEN Chu-jing, LIU Wei, WANG Gang, HE Ru-jie. Additive manufacturing of fiber reinforced ceramic matrix composites: Advances, challenges, and prospects [J]. Ceramics International, 2022, 48(14): 19542−19556.

[8] TULI N T, KHATUN S, RASHID A B. Unlocking the future of precision manufacturing: A comprehensive exploration of 3D printing with fiber-reinforced composites in aerospace, automotive, medical, and consumer industries [J]. Heliyon, 2024, 10(5): e27328.

[9] YI Xu, TAN Zhou-jian, YU Wan-jing, LI Jun, LI Bing-ju, HUANG Bo-yun, LIAO Ji-qiao. Three dimensional printing of carbon/carbon composites by selective laser sintering [J]. Carbon, 2016, 96: 603−607.

[10] WANG Jia-chang, DOMMATI H, HSIEH S J. Review of additive manufacturing methods for high-performance ceramic materials [J]. The International Journal of Advanced Manufacturing Technology, 2019, 103(5/6/7/8): 2627−2647.

[11] LIU Kai, WANG Jiang, WU Tian, SUN Hua-jun. Effects of carbon content on microstructure and mechanical properties of SiC ceramics fabricated by SLS/RMI composite process [J]. Ceramics International, 2020, 46(14): 22015−22023.

[12] XU Teng-teng, CHENG Su, JIN Lai-Zhen, ZHANG Kun, ZENG Tao. High-temperature flexural strength of SiC ceramics prepared by additive manufacturing [J]. International Journal of Applied Ceramic Technology, 2020, 17(2): 438−448.

[13] CHEN Xiao, YIN Jie, LIU Xue-jian, PEI Bing-bing, HUANG Jian, PENG Xing-lin, XIA Ai-dong, HUANG Long-zhi, HUANG Zheng-ren. Effect of laser power on mechanical properties of SiC composites rapidly fabricated by selective laser sintering and direct liquid silicon

infiltration [J]. Ceramics International, 2022, 48(13): 19123−19131.

[14] COSTAKIS W J, RUESCHHOFF L M, DIAZ-CANO A I, YOUNGBLOOD J P, TRICE R W. Additive manufacturing of boron carbide via continuous filament direct ink writing of aqueous ceramic suspensions [J]. Journal of the European Ceramic Society, 2016, 36(14): 3249−3256.

[15] KEMP J W, DIAZ A A, MALEK E C, CROOM B P, APOSTOLOV Z D, KALIDINDI S R, COMPTON B G, RUESCHHOFF L M. Direct ink writing of $ZrB_2$−SiC chopped fiber ceramic composites [J]. Additive Manufacturing, 2021, 44(Suppl C): 102049.

[16] RUESCHHOFF L, COSTAKIS W, MICHIE M, YOUNGBLOOD J, TRICE R. Additive manufacturing of dense ceramic parts via direct ink writing of aqueous alumina suspensions [J]. International Journal of Applied Ceramic Technology, 2016, 13(5): 821−830.

[17] FRANCHIN G, WAHL L, COLOMBO P. Direct ink writing of ceramic matrix composite structures [J]. Journal of the American Ceramic Society, 2017, 100(10): 4397−4401.

[18] KEMP J W, HMEIDAT N S, COMPTON B G. Boron nitride-reinforced polysilazane-derived ceramic composites via direct-ink writing [J]. Journal of the American Ceramic Society, 2020, 103(8): 4043−4050.

[19] XIONG Hui-wen, ZHAO Lian-zhong, CHEN He-hao, LUO Hang, YUAN Xi, ZHOU Ke-chao, ZHANG Dou. Building SiC-based composites from polycarbosilane-derived 3D-SiC scaffolds via polymer impregnation and pyrolysis (PIP) [J]. Journal of the European Ceramic Society, 2021, 41(2): 1121−1131.

[20] FRANCHIN G, MADEN H S, WAHL L, BALIELLO A, PASETTO M, COLOMBO P. Optimization and characterization of preceramic inks for direct ink writing of ceramic matrix composite structures [J]. Materials, 2018, 11(4): 515.

[21] WANG Wen-qing, GAO Xiong, ZHANG Lu, MA Qing-song, LI Su-wen, LI Zeng-chan, SHEN Chu-jing, WANG Gang, HE Ru-jie. Large-scale material extrusion-based additive manufacturing of short carbon fibre-reinforced silicon carbide ceramic matrix composite preforms [J]. Virtual and Physical Prototyping, 2023, 18(1): e2245801.

[22] LEWICKI J P, RODRIGUEZ J N, ZHU Cheng, WORSLEY M A, WU A S, KANARSKA Y, HORN J D, DUOSS E B, ORTEGA J M, ELMER W , HENSLEIGH R, FELLINI R A, KING M J. 3D-printing of meso-structurally ordered carbon fiber/polymer composites with unprecedented orthotropic physical properties [J]. Scientific Reports, 2017, 1(1): 43401.

[23] XIA Yuan-lin, LU Zhong-liang, CAO Ji-wei, MIAO Kai, LI Jian, LI Di-chen. Microstructure and mechanical property of $C_f$/SiC core/shell composite fabricated by direct ink writing [J]. Scripta Materialia, 2019, 165: 84−88.

[24] CLARKSON C M, WYCKOFF C, COSTAKIS W, ABBOTT A, SCHLUP A, KEMP J W, RUESCHHOFF L M, DICKERSON M B, KOERNER H. Phenolic carbon fiber composite inks for the additive manufacturing of carbon/carbon (C/C) [J]. Additive Manufacturing, 2024, 83: 104056.

[25] HMEIDAT N S, KEMP J W, COMPTON B G. High-strength epoxy nanocomposites for 3D printing [J]. Composites Science and Technology, 2018, 160: 9−20.

[26] ROMBERG S K, ISLAM M A, HERSHEY C J, DEVINNEY M, DUTY C E, KUNC V, COMPTON B G. Linking thermoset ink rheology to the stability of 3D-printed structures [J]. Additive Manufacturing, 2021, 37: 101621.

[27] SMAY J E, CESARANO III J., LEWIS J A. Colloidal inks for directed assembly of 3-D periodic structures [J]. Langmuir, 2002, 18(14): 5429−5437.

[28] ZHANG Ke-qiang, HE Ru-jie, XIE Chen, WANG Gang, DING Guo-jiao, WANG Min, SONG Wei-dong, FANG Dai-ning. Photosensitive $ZrO_2$ suspensions for stereo-lithography [J]. Ceramics International, 2019, 45(9): 12189−12195.

[29] LI Wen-dong, WANG Chao, JIANG Zhi-hui, CHEN Lun-jiang, WEI Yan-hui, ZHANG Li-yuan, CHEN Ming-yu, YANG Xiong, ZHANG Guan-jun. Stereolithography based additive manufacturing of high-*k* polymer matrix composites facilitated by thermal plasma processed barium titanate microspheres [J]. Materials & Design, 2020, 192: 108733.

[30] CHAUVETTE J F, HIA I L, FARAHANI R D, PLANTE R, PICCIRELLI N, THERRIAULT D. Non-planar multinozzle additive manufacturing of thermoset composite micro-scaffold networks [J]. Composites Part B: Engineering, 2023, 256: 110627.

[31] JIANG Feng-ze, ZHOU Ming-yong, DRUMMER D. Effects of fumed silica on thixotropic behavior and processing window by UV-assisted direct ink writing [J]. Polymers, 2022, 14(15): 3107.

[32] WANG Hao-huan, HUANG Zheng-yong, ZHANG Ying-fan, LI Li-cheng, LI Jian. Design of enhanced mechanical properties by interpenetrating network of 3D printing dual-curing resins [J]. Polymer, 2023, 282: 126153.

[33] SCHWARZER-FISCHER E, ZSCHIPPANG E, KUNZ W, KOPLIN C, LÖW Y M, SCHEITHAUER U, MICHAELIS A. CerAMfacturing of silicon nitride by using lithography-based ceramic vat photopolymerization (CerAM VPP) [J]. Journal of the European Ceramic Society, 2023, 43(2): 321−331.

[34] ZHU Cheng, SMAY J E. Catenary shape evolution of spanning structures in direct-write assembly of colloidal gels [J]. Journal of Materials Processing Technology, 2012, 212(3): 727−733.

[35] KEMP J W, REED J L, COMPTON B G. Size effects in 3D-printed polymer-derived, zirconium diboride-reinforced ceramic composites [J]. Journal of the American Ceramic Society, 2024, 107(3): 1557−1570.

[36] PUPIN C, ROSS A, DUBOIS C, RIETSCH J C, RUIZ E. Predicting porosity formation in phenolic resins for RTM manufacturing: The porosity map [J]. Composites Part A: Applied Science and Manufacturing, 2017, 100: 294−304.

# 碳/碳复合材料双固化墨水直写成型的流变特性、固化行为与孔隙演变

叶 鑫[1]，卢 谦[1]，伍璐彤[1]，徐明亮[2]，熊 翔[2]，蒋丰泽[2]

1. 中南大学 机电工程学院，长沙 410083；
2. 中南大学 粉末冶金国家重点实验室，长沙 410083

**摘 要**：为克服传统 C/C 复合材料制备对模具的依赖以及复杂几何形状制造的困难，采用紫外光/热双固化直写成型(DIW)技术制备高性能 C/C 复合材料。系统分析了复合墨水的流变特性，以探明酚醛树脂(PR)与碳纤维(CF)含量的影响。结果表明，复合墨水表现出显著的剪切变稀行为与强触变性，为实现稳定的成型提供了可靠保障。此外，探究了材料的紫外光/热固化行为，为优化固化参数提供了理论依据。研究发现，与纯 PR 相比，CF 的加入显著降低了紫外光穿透能力；随着 CF 含量的增加，其临界紫外线照射能量从 68.47 mJ/cm$^2$ 迅速增加至 911.19 mJ/cm$^2$，这种显著变化凸显成型工艺优化的重要性。在此基础上，利用碳管炉对成型构件进行热解，制备了 C/C 复合材料预制体，并探讨孔隙形成特征。通过化学气相渗透(CVI)技术填补热解过程中产生的孔隙，改善 C/C 复合材料的性能，其弯曲强度提高至 115.19 MPa。

**关键词**：C/C 复合材料；双重固化；墨水直写；流变特性；固化行为；化学气相渗透

**(Edited by Bing YANG)**